



Analytical and numerical study of the ground-track
resonances of Dawn orbiting Vesta

by Nicolas Delsate

Report naXys-04-2011

21 January 2011



Namur Center for Complex Systems

University of Namur

8, rempart de la vierge, B5000 Namur (Belgium)

<http://www.naxys.be>

Abstract

The aim of Dawn mission is the acquisition of data from orbits around two bodies, (4) Vesta and (1) Ceres, the two most massive asteroids.

Due to the low thrust propulsion, Dawn will slowly cross and transit through ground-track resonances, where the perturbations on Dawn orbit may be significant. In this context, to safely go the Dawn mission from the approach orbit to the lowest science orbit, it is essential to know the properties of the crossed resonances.

This paper analytically investigates the properties of the major ground-track resonances (1:1, 1:2, 2:3 and 3:2) appearing for Vesta orbiters: location of the equilibria, aperture of the resonances and period at the stable equilibria. We develop a general method using an averaged Hamiltonian formulation with a spherical harmonic approximation of the gravity field. If the values of the gravity field coefficient change, our method stays correct and applicable. We also discuss the effect of one error on the C_{20} and C_{22} coefficients on the properties of the 1:1 resonance. These results are checked by numerical tests. We determine that the increase of the eccentricity appearing in the 2:3 resonance is due to the J_{22} coefficient. Finally we numerically study the probability of the capture in resonance 1:1. Our paper reproduces, explains and completes the results of Tricarico and Sykes (2010).

Keyword Vesta – Gravitational perturbations – Resonance – Spacecraft operations – Analytical study

1 Introduction

After the explorations of the planet of our Solar System, the new space missions are aimed at asteroids and comets, moving from fly-bys to rendezvous and orbiting. For these missions the space probe could have an operating orbital period close to the asteroid one. A challenge for the navigators of these missions is to predict the orbital environment around the asteroid and to derive pre-mission plans for the control of these orbits.

Several authors have already been interested in these problems. Scheeres (1994) studied the stability of a spacecraft in synchronous orbits with the asteroid rotation. Scheeres et al. (1998) presented the dynamics of orbits close to the asteroid 4179 Toutatis. Rossi et al. (1999) numerically studied the orbital evolution around irregular bodies with two methods. The first is based on a representation of the central body in terms of “mascons”, and the second model considers the central body as a polyhedron with a variable number of triangular faces. Hu and Scheeres (2002) investigated

the spacecraft motion about a slowly rotating asteroid (as compared to the spacecraft orbit period) with the second degree and order of the gravity field. Lara et al. (2010) and Russell and Lara (2009) were interested in the motion of an orbiter around Enceladus. More recently, Tricarico and Sykes (2010) studied the dynamical environment of Dawn around Vesta.

The asteroid (4) Vesta is one of the biggest minor planets of the main belt. Originally discovered in 1807 by Heinrich Olbers, it is one of the targets of the space mission Dawn (Rayman et al., 2006; Russell et al., 2007), that will perform three different altitude science orbits before flying to Ceres. Dawn was successfully launched on September 27, 2007 and will arrive to Vesta in July 2011. In the preparation of this mission, Tricarico and Sykes (2010) proposed a numerical survey of the orbits around Vesta and emphasized particularly the problem of the 1:1 ground-track resonance.

We revisit their study in adding a more complete numerical exploration and analytical explanations of the observed phenomena i.e. location, aperture and period of the stable equilibria of the ground-track resonances. The interest of an analytical investigation is the easiness and the fastness to refine the results when the data change.

Our paper is organized as follows. In section 2 we briefly recall the specification of the Dawn mission and we determine the main forces acting on Dawn orbiting Vesta. Then we select the most important perturbations that we use in our analytical models. In section 3 we rebuild the results of Tricarico and Sykes (2010) and we numerically localize the ground-track resonances (the commensurabilities between the orbital period of the probe and the rotational period of the asteroid); we measure the aperture of these resonances and we determine the period at the stable equilibrium of the 1:1 resonance. In section 4 we recover the results of section 3 but in a purely analytical way. We develop a general method using an averaged Hamiltonian formulation with a spherical harmonic approximation of the gravity field. We also discuss the effect of an error on the C_{20} and C_{22} coefficients on the properties of the 1:1 resonance. In section 5 we show that the increase of the eccentricity in the 2:3 resonance is due to the J_{22} coefficient. In section 6 we study numerically the thrust and the probability of capture in the 1:1 resonance and we detail the results of Tricarico about the trapping. Finally we summarize and draw our conclusions.

2 Main perturbations acting on Dawn around Vesta

2.1 Dawn mission

Dawn will be the first mission to orbit two main belt asteroids: Vesta and Ceres. They are the two most massive asteroids in the main belt and they are particularly interesting because they span the region of space between the rocky inner body Solar System and the wetter bodies of the outer Solar System. They have survived intact from the earliest days of the Solar System. Hence they can provide the opportunity for acting as windows to the conditions present in the first few millions years of the Solar System existence.

For a complete overview of the Dawn mission, we refer to Rayman et al. (2006) and Russell et al. (2007). The science observations will be concentrated in three campaigns around Vesta, each one conducted in a different circular, Sun-synchronous quasi-polar orbit. The first science orbit, Vesta Science Orbit 1 (VSO1), has a radial distance of 2 700 km (corresponding to an equatorial altitude of about 2 400 km) with a period of 58 hours. Upon completion of VSO1, the thrusting will resume for the 3-week transfer to Vesta Science Orbit 2 (VSO2). The VSO2 distance is 950 km (an equatorial altitude about 670 km), where the orbital period is 12 hours. This part of the mission is named HAMO, namely High Altitude Mapping Orbit. The transfer from VSO2 to VSO3 will take 30 days. At a radial distance of 460 km (equatorial altitude of about 180 km), VSO3 is the lowest orbit planned and its orbital period is 4 hours. This last scientific orbit is named LAMO for Low Altitude Mapping Orbit. The transition between the different phases are made by a Solar electric propulsion with low thrust.

2.2 Main perturbations

The major perturbations acting on a probe orbiting an asteroid of the main belt are due to the discrepancies of the asteroid gravitational field, to the gravitational perturbations induced by the Sun, Mars and Jupiter as well as to the direct radiation pressure of the Sun. We use the following simplified relations (Montenbruck and Eberhard, 2000) to characterize the norms of

the accelerations induced by these 3 forces:

$$\begin{aligned}
 a_{nm} &= (n+1) \frac{\mu}{r^2} \frac{R_e^n}{r^n} \sqrt{\bar{C}_{nm}^2 + \bar{S}_{nm}^2}, \\
 a_{3b} &= \frac{2\mu_{3b}}{d_{3b}^3} r, \\
 a_{rp} &= C_r \frac{A}{m} P_{\odot}
 \end{aligned} \tag{1}$$

where a_{nm} is proportional to the coefficient of degree n and order m of the spherical harmonic development; a_{3b} corresponds to the acceleration induced by the third body (Sun, Mars or Jupiter) and a_{rp} is the acceleration due to the direct radiation pressure. R_e is the equatorial radius of the asteroid, \bar{C}_{nm} and \bar{S}_{nm} are the normalized coefficients of the gravitational potential; μ and μ_{3b} represent the gravitational constants of the asteroid (Vesta or Ceres) and of the third body respectively. $P_{\odot} = 4.56 \times 10^{-6} \text{N/m}^2$ is the radiation pressure for an object located at a distance of 1 AU from the Sun and C_r is the reflectivity coefficient appearing in the direct radiation pressure acceleration. A/m is the area-to-mass ratio, d_{3b} is the distance between the object and the third body and r is the distance between the probe and the central body (asteroid). The A/m of Dawn is approximately equal to $0.04 \text{ m}^2/\text{kg}$ (Tricarico and Sykes, 2010). The values of the coefficients $\bar{C}_{nm}, \bar{S}_{nm}$ that we use can be found in Table 1 of Tricarico and Sykes (2010) as well as the values of $a_{3b} = 2.36 \text{ UA}$ and $R_e = 300 \text{ km}$.

We draw the order of magnitude of the main perturbations (1) as functions of the “planetocentric” satellite distance r in Fig. 1. As a consequence of the location ($\sim 2.5 \text{ UA}$) and the shape of the asteroid (Vesta and Ceres) the order of magnitude of the perturbations is relatively different from the magnitude of the perturbations for a satellite of the Earth. For a space probe orbiting Ceres or Vesta, the perturbation due to the discrepancies of the gravitational field is several orders of magnitude greater than these due to the third body (or to the radiation pressure) perturbations. This remains true for large values of the probe semi-major axis. On the contrary, in the case of a stationary satellite of the Earth (GEO), the Luni-Solar perturbations are comparable in size to the Earth oblateness ones.

Therefore, later in this paper, we shall only keep the perturbations due to the gravitational field of the asteroid.

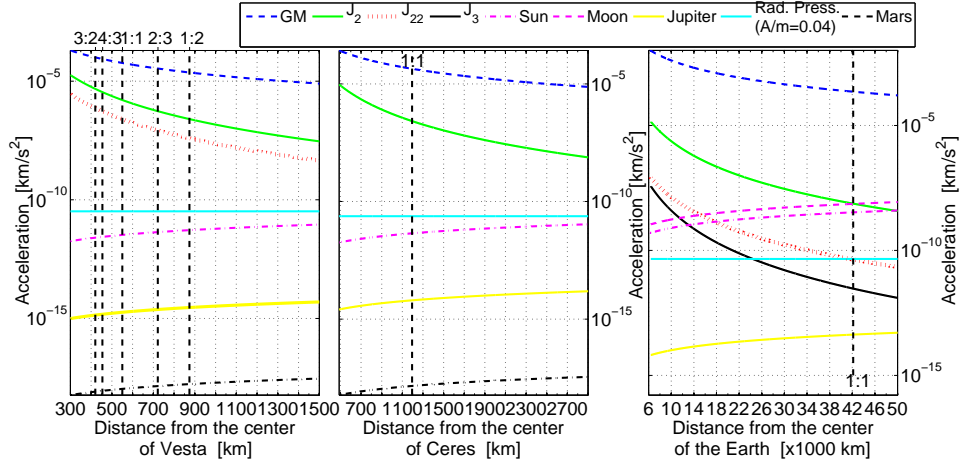


Figure 1: The orders of magnitude of the main perturbations acting on a probe around Vesta and Ceres (left and central panel) and, comparatively, around the Earth. The dashed vertical lines show the “geo”stationary and “asterostationary” semi-major axis.

3 Vesta dynamical environment: numerical study

The effects due to a non-spherical asteroid shape are quite complex. Several authors gave different solutions to modelize the asteroid gravitational field. Rossi et al. (1999) used the mascons or the polyhedrons approximations. Scheeres (1994) and Compere et al. (2011) used a tri-axial ellipsoid representation. Let us note that the spherical harmonic representation of the gravity field is uniformly convergent for $a < c\sqrt{2}$ (Balmino, 1994; Pick et al., 1973) where a and c are the biggest and smallest semi-axis of the asteroid. This is the case of Vesta. Then the major gravitational perturbations of the asteroid shape onto the orbit of an orbiter can usually be characterized by the spherical harmonics. For example, to characterize the main effect of the asteroid shape, it is convenient to use the primary oblateness term C_{20} .

Furthermore, using a spherical harmonic representation, Tricarico and Sykes (2010) tested several models for the mass density distribution of Vesta. They concluded that Dawn dynamics depends primarily on Vesta shape and only secondarily on the details of the interior structure. Therefore we decide to use the uniform mass density scenario of Tricarico with a spherical harmonic development of the gravity field.

As previously stated, the dynamics of a spacecraft orbiting within ~ 1000 km from Vesta is dominated by the gravitational field of Vesta. As a consequence the system of differential equations describing the probe motion is given by $\ddot{\mathbf{r}} = -\nabla U_{\text{pot}}$, where $\ddot{\mathbf{r}}_{\text{pot}}$ represents the acceleration induced by Vesta gravity field and can be expressed as the gradient of the following potential (Kaula, 1966)

$$U_{\text{pot}}(r, \delta, \phi) = -\frac{\mu}{r} + \frac{\mu}{r} \sum_{n=2}^{\infty} \sum_{m=0}^n \left(\frac{R_e}{r}\right)^n \mathcal{P}_n^m(\sin \phi) (C_{nm} \cos m\delta + S_{nm} \sin m\delta), \quad (2)$$

where the quantities C_{nm} and S_{nm} are the spherical harmonics coefficients of the potential of Vesta. n and m are respectively the degree and the order of the development. μ and R_e are respectively the gravitational constant and equatorial radius of Vesta. The quantities (r, δ, ϕ) describe the planetocentric spherical coordinates of the space probe. \mathcal{P}_n^m are the associated Legendre polynomials. It is worth noting that all terms S_{n0} are zero. The potential (2) may be expressed using an alternative way, with a cosine terms, introducing a phase difference δ_{nm} as well as a coefficient J_{nm} :

$$U_{\text{pot}}(r, \delta, \phi) = -\frac{\mu}{r} - \frac{\mu}{r} \sum_{n=2}^{\infty} \sum_{m=0}^n \left(\frac{R_e}{r}\right)^n \mathcal{P}_n^m(\sin \phi) (J_{nm} \cos(m\delta - m\delta_{nm})), \quad (3)$$

where

$$C_{nm} = -J_{nm} \cos(m\delta_{nm}), \quad S_{nm} = -J_{nm} \sin(m\delta_{nm}), \quad m\delta_{nm} = \arctan\left(\frac{-S_{nm}}{-C_{nm}}\right). \quad (4)$$

Tricarico and Sykes (2010) have shown that the dynamical behavior of Dawn is dominated by the first 8 degrees of the gravitational potential and that the main resonant terms are of degree 3 and 4. Henceforth we model the gravity potential of the central body using the coefficients until degree and order 4. The coefficients used here can be found in the Table 1 of Tricarico and Sykes (2010).

The numerical integrations of the differential equations are made by a home-made numerical software: **N**umerical **I**ntegration of the **M**otion of an **A**rtificial **S**atellite orbiting a **T**elluric **P**lanet, for short **NIMASTEP**. This extensive tool allows to derive the osculating motion of an arbitrary object orbiting any of the terrestrial planets of our Solar System. This software has been elaborated by N. Delsate and successfully used in Valk et al. (2009b) and Delsate et al. (2010). It has been recently extended for asteroids in Compere et al. (2011).

3.1 Maps of variation of semi-major axis, inclination and radial distance

In Fig. 2, we plot the results of the numerical integrations performed for a set of 316 800 orbits, propagated over a time span of 1 year with a entry-level step size of 100 seconds. We consider a set of initial conditions defined by a mean anomaly grid of 1° and a semi-major axis grid of 700 m, spanning the [385, 1 001] km range. In this work, we explore the dynamics of the spacecraft Dawn in a polar orbit ($i_0 = 90^\circ$) because the initial inclination of Vesta is Sun-synchronous, thus corresponds to a quasi-polar orbit. The other fixed initial conditions are $\Omega = \omega = 0^\circ$ for the longitude of the ascending node and the argument of pericenter respectively, and $\theta = 0^\circ$ for the sidereal time.

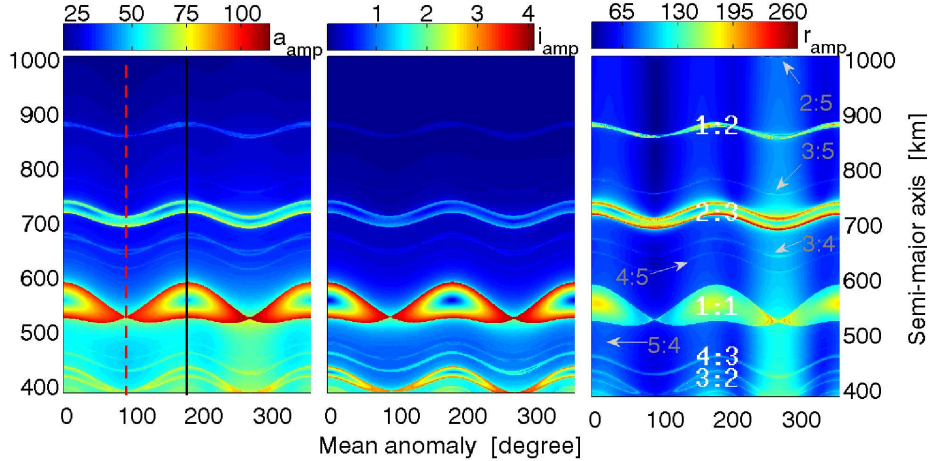


Figure 2: The semi-major axis, the inclination and the radial distance computed as functions of the initial mean anomaly and the initial semi-major axis. The equations of motion include the central body attraction, the harmonics until degree and order 4. The anomaly step is 1° and the semi-major axis step is 700 m. The initial conditions are $i_0 = 90^\circ$, $\Omega = \omega = 0^\circ$ and $\theta = 0^\circ$. The integration time is 1 year. The patterns have been obtained by plotting the amplitude of variation of the semi-major axis (a_{amp}) in the left panel, the amplitude of variation of the inclination (i_{amp}) in the central panel and the amplitude of variation of the radial distance in the right panel (r_{amp}). These amplitude are shown by the colorbars.

We show the amplitude of the semi-major axis (namely the difference

between the maximum and minimum semi-major axis reached during the integration), inclination and radial distance of each orbit respectively in the left, central and right panels of Fig. 2. These figures allow to locate the *ground-track* resonances. Indeed, when the orbital period of the space probe is close to a commensurability with the rotational period of Vesta, the repeating ground-track of the probe will periodically encounter the same configuration of the gravitational field. This is what we call a *ground-track resonance*. Then a part of the effects of the gravitational perturbations is amplified leading to a motion with very long periods and large perturbations in the semi-major axis of the spacecraft orbit. This is what we observe in the left panel of Fig. 2 where the variation of the semi-major axis is clearly largest at ~ 550 km and ~ 720 km, as shown by the color code.

It is obvious that the usual pendulum-like phase spaces (Gedeon, 1969) (appearing in the case of a ground-track resonance) are distorted like a wave. Actually, it is worth noting that, at first, the sampling is carried out with respect to the osculating initial conditions. Second, within the framework of mean motion theory, it is well-known (Exertier and Métris, 1995) that, due to the short-period oscillations, the mean and the osculating initial conditions cannot be considered as equal. In other words, for the same fixed value of the initial osculating semi-major axis and for various initial mean anomalies, we obtain different values for the mean semi-major axis. For more explanation, in a geostationary satellite case, the reader can refer to Valk et al. (2009b).

The results obtained here are similar to Tricarico and Sykes (2010) ones (Fig.4 in their article). We easily find 5 main ground-track resonances (noted in white in Fig. 2): 3:2, 4:3, 1:1, 2:3 and 1:2. It is also possible to find other resonances (5:4, 4:5, 3:4, 5:3 and 5:2) but they are very thin (noted in gray with an arrow in Fig. 2). The amplitude of variation of the inclination is near 1° , except around the separatrix of the 1:1 resonance where the amplitude of variation reaches 3.8° . In consequence, in the future, we shall consider the inclinations as equal to 90° . In the right panel of Fig. 2, we notice that the two most important resonances are the 1:1 and the 2:3 resonances: the largest is the 1:1 but the strongest perturbations on the radial distance appear in the 2:3 resonance. This last observation will be explained in this paper (Section 5).

3.2 Location and aperture of the main ground-track resonances

Now let us determine the location and the aperture of the main resonances. We perform two initial mean anomaly sections (Fig. 2) near a stable (vertical continued black line) and an unstable (dashed red line) equilibrium point of the resonance 1:1. For each orbit of these two sections, we compute, using the

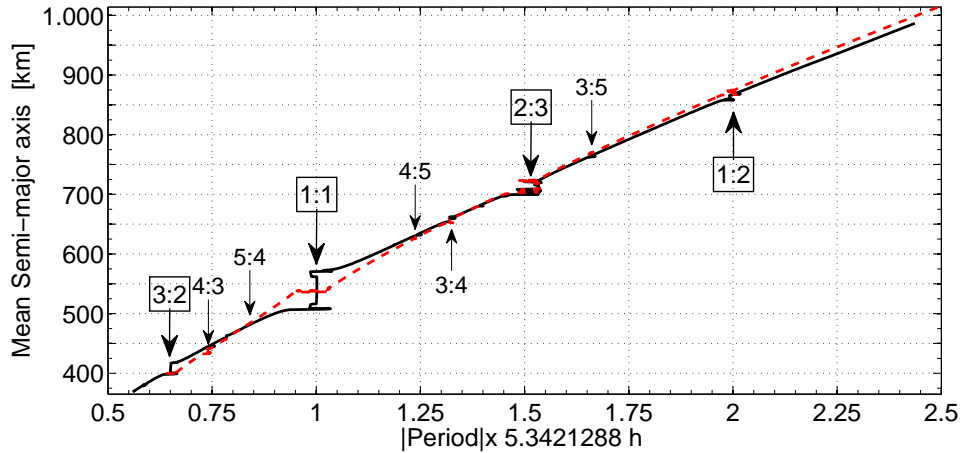


Figure 3: The mean semi-major axis of a probe around Vesta with respect to its mean anomaly period. The periods are obtained by frequency analysis (NAFF). The estimation of the periods is made over a period of 1 year. The model used is the same as in Fig. 2. The continued black and the dashed red lines correspond to the vertical lines of Fig. 2 (left panel). We tick off the detectable ground-track resonances.

Numerical Analysis of Fundamental Frequencies, for short NAFF (Laskar, 1988, 2005), the fundamental period of the mean anomaly with respect to the mean initial semi-major axis a_0 . The mean semi-major axis is calculated with a numerical averaging method applied on the osculating semi-major axis, on 5 revolutions of Dawn around Vesta. The results are presented in Fig. 3 and in Tab. 1. For more explanations and other applications of the using of NAFF in space geodesy we refer to Lemaître et al. (2009).

Table 1: The mean semi-major axis location and the aperture of the main resonances (using Fig. 3).

Resonance	3:2	1:1	2:3	1:2
Mean Semi-major axis [km]	409.1	539.6	717.3	871.5
Aperture [km]	18	63	22.5	7.5

3.3 Period of the resonant angle at the stable equilibrium of the 1:1 resonance

In the case of a 1:1 ground-track resonance, the resonant angle is defined by $\sigma = \lambda - \theta = (\Omega + \omega + M) - \theta$ where θ is the sidereal time (Gedeon, 1969; Valk et al., 2009a), λ is the mean longitude, Ω is the ascending node, ω is the argument of pericenter and M is the mean anomaly. For illustration, we draw in Fig. 4 the motion of a probe in resonance 1:1 with its central body.

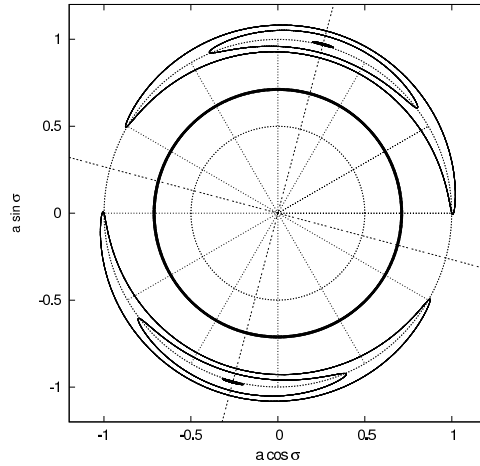


Figure 4: General illustration of the motion of a 1:1 ground-track resonant probe near stable equilibria in a rotating reference frame as seen from the pole. The variations on the mean semi-major axis have been amplified for the illustration.

We can determine the period of the resonant angle σ at the center of the banana curves. For that, we use the **N**amur **A**lgorithm **F**or **F**orced **O**scillations, for short **NAFFO** (Noyelles et al., 2011), to determine numeri-

cally the semi-major axis and the value of the resonant angle corresponding to the stable equilibrium. For clarity, the algorithm is reminded here: the initial conditions (a, σ) are conveniently chosen to be close enough to the equilibrium, here for example $a = 550$ km and $\sigma = 90^\circ$. Now we try to minimize the free libration (the oscillation of σ and a in the banana curves). This minimization is performed iteratively by

- (1) performing a numerical integration of the equations of the motion;
- (2) identifying the free component by a frequency analysis (here using NAFF);
- (3) removing the free component from the initial conditions to determine a new initial condition. Then a new numerical integration is being performed (return to step 1).

We apply this algorithm to different models containing only the gravity field of the central body. They respectively contain the J_{22} term (J_{nm} are defined by Eq. (4)), the J_{22} and J_2 terms ($-C_{20} = J_{20} \stackrel{\text{not.}}{=} J_2$), and finally the whole gravity field until degree and order 4 ($n = 4 = m$). When the algorithm stops, we make a frequency analysis (NAFF) of the signal (a, σ) to determine the period of the resonant angle at the equilibrium.

The results of NAFFO are summarized in Tab. 2. Let us note that we calculate an average of the resonant angle and of the semi-major axis with respect to the time to obtain a *mean* value. The 11.21 km difference between the J_{22} and the $J_{22} + J_2$ model underlines the fact that the J_2 term induces an important shift on the semi-major axis location.

Table 2: Numerical study of the location of the 1:1 resonant for different models. The first two lines are given by the NAFFO algorithm. The *mean* semi-major axis and the *mean* resonant angle are obtained by numerical average with respect to the time. The third line is obtained using NAFF.

Model	J_{22}	$J_2 + J_{22}$	All until $n = m = 4$
<i>Mean</i> semi-major axis (km)	549.63	538.42	538.89
<i>Mean</i> resonant angle σ (degree)	90°	90.814°	91.144°
Period (day)	2.45	2.47	2.56

Our semi-major axis location of the 1:1 stable equilibria shows a good agreement with Fig. 4 of Tricarico and Sykes (2010). For the period of the

resonant angle, Tricarico and Sykes (2010) obtained a value close to 2.5 days (Fig. 8 in their article) that coincides well with our result. Remark that, for this main resonance, our numerical simplified model $J_2 + J_{22}$ obtains a good approximation of the stable equilibrium location and of the resonant angle period.

4 Ground-track resonances: analytical study

In this section, we study analytically the main ground-track resonances (1:1, 1:2, 2:3 and 3:2) found in the previous section. First, we present a general Hamiltonian describing the motion of a probe orbiting an irregular central body. Then, we identify the main ground-track resonances. For each of them we simplify the Hamiltonian in the circular polar case, we explain the resonant angle, we determine the location and the aperture of the resonance and we calculate the period of the resonant angle at the stable equilibrium. The results are compared with the previous numerical results.

For the 1:1 resonance we also study the circular equatorial case for comparison and we investigate the effect of an error on C_{20} and C_{22} on the properties of the resonance.

4.1 Hamiltonian in terms of the orbital elements and condition for ground-track resonances

The potential (2) may be expressed using an alternative way, with the satellite orbital elements $(a, e, i, \Omega, \omega, M)$ and the sidereal time θ , Kaula (1966) represents the gravitational field as

$$U = -\frac{\mu}{r} + \sum_{n=2}^{\infty} \sum_{m=0}^n \sum_{p=0}^n \sum_{q=-\infty}^{+\infty} \frac{\mu}{a} \left(\frac{R_e}{a}\right)^n F_{nmp}(i) G_{npq}(e) S_{nmpq}(\Omega, \omega, M, \theta), \quad (5)$$

where the functions S_{nmpq} depend on the gravity field coefficient C_{nm} and S_{nm} ,

$$S_{nmpq}(\Omega, \omega, M, \theta) = \begin{cases} +C_{nm} \\ -S_{nm} \end{cases}_{n-m \text{ odd}}^{n-m \text{ even}} \cos \Theta_{nmpq}(\Omega, \omega, M, \theta) \\ + \begin{cases} +S_{nm} \\ +C_{nm} \end{cases}_{n-m \text{ odd}}^{n-m \text{ even}} \sin \Theta_{nmpq}(\Omega, \omega, M, \theta), \quad (6)$$

where n, m, p, q are integers, θ is the sidereal time and

$$\Theta_{nmpq}(\Omega, \omega, M, \theta) = (n - 2p)\omega + (n - 2p + q)M + m(\Omega - \theta) \quad (7)$$

is Kaula's gravitational argument.

$F_{nmp}(i)$ and $G_{npq}(e)$ are respectively the inclination and eccentricity functions. To have a complete list of the values of these functions, we refer to Kaula (1966) and Chao (2005). The third index q of the eccentricity functions determines the lowest power of the eccentricity appearing in the potential.

With the momentum $L = \sqrt{\mu a}$ conjugated to $\lambda = \Omega + \omega + M$ the Hamiltonian describing the motion of a probe around an irregular central body is given by

$$\mathcal{H} = -\frac{\mu^2}{2L^2} + \sum_{n=2}^{\infty} \sum_{m=0}^n \sum_{p=0}^n \sum_{q=-\infty}^{+\infty} R_e^n \frac{\mu^{n+2}}{L^{2n+2}} F_{nmp}(i) G_{npq}(e) S_{nmpq}(\Omega, \omega, M, \theta) + \dot{\theta}\Lambda. \quad (8)$$

$\dot{\theta}\Lambda$ is due to the asteroid rotation, the quantity Λ is the momentum conjugate to the sidereal time θ .

The ground-track resonances occur when the rate of Kaula gravitational argument is close to zero, that is

$$\dot{\Theta}_{nmpq}(\dot{\Omega}, \dot{\omega}, \dot{M}, \dot{\theta}) = (n - 2p)\dot{\omega} + (n - 2p + q)\dot{M} + m(\dot{\Omega} - \dot{\theta}) \simeq 0 \quad (9)$$

where p and q are small integer numbers.

4.2 Resonance 1:1

A similar (more detailed) work has been performed in Valk et al. (2009a). In this paper the authors studied the geostationary space debris ($e = 0$, $i = 0^\circ$) without taking into account the J_2 term.

It is well know (Gedeon, 1969; Scheeres, 1994; Valk et al., 2009a) that the resonance 1:1 is due to the second degree and order of the gravity field. From Eq. (8), let us write the Hamiltonian of the second order and degree harmonic, denoted by $\mathcal{H}_{1:1}$:

$$\mathcal{H}_{1:1} = -\frac{\mu^2}{2L^2} + \sum_{m=0}^2 \sum_{p=0}^2 \sum_{q=-\infty}^{+\infty} R_e^2 \frac{\mu^4}{L^6} F_{2mp}(i) G_{2pq}(e) S_{2mpq}(\Omega, \omega, M, \theta) + \dot{\theta}\Lambda \quad (10)$$

with $\Theta_{2mpq} = 2(1-p)\omega + (2-2p+q)M + m(\Omega - \theta)$. We consider the z-axis as aligned with the asteroid main axis of inertia ($C_{21} = 0 = S_{21}$), $q = 0$ (null eccentricity) and the resonant condition (9) becomes: $p = 1 - \frac{m}{2}$; then the Hamiltonian writes ($S_{20} = 0$):

$$\begin{aligned} \mathcal{H}_{1:1} = & -\frac{\mu^2}{2L^2} + R_e^2 \frac{\mu^4}{L^6} \left[F_{201}(i) G_{210}(e) C_{20} \cos(\Theta_{2010}) \right. \\ & \left. + F_{220}(i) G_{200}(e) \left(C_{22} \cos(\Theta_{2200}) + S_{22} \sin(\Theta_{2200}) \right) \right] + \dot{\theta} \Lambda \end{aligned} \quad (11)$$

where Θ_{nmpq} , $F_{nmp}(i)$ and $G_{npq}(e)$ are presented in Tab. 3.

Table 3: Expression of the functions Θ_{nmpq} , $F_{nmp}(i)$ and $G_{npq}(e)$ with respect to the values of $n = 2$, $m \in \{0, 2\}$, $p = 1 - m/2$ and $q = 0$.

n	m	p	q	Θ_{nmpq}	$F_{nmp}(i)$	$G_{npq}(e)$
2	0	1	0	0	$\frac{3}{4} \sin^2 i - \frac{1}{2}$	$\frac{1}{(1-e^2)^{\frac{3}{2}}}$
2	2	0	0	$2\omega + 2M + 2(\Omega - \theta)$	$\frac{3}{4}(1 + \cos i)^2$	$(1 - \frac{5}{2}e^2 + \frac{13}{16}e^4 + \dots)$

Let us define the so-called resonant angle σ (Gedeon, 1969; Scheeres, 1994; Valk et al., 2009a)

$$\sigma = \lambda - \theta = (\Omega + \omega + M) - \theta. \quad (12)$$

In order to keep a canonical set of variables, we use a symplectic transformation leading to the new set of canonical variables

$$\sigma, \quad L' = L, \quad \theta' = \theta, \quad \Lambda' = \Lambda + L. \quad (13)$$

Then the Hamiltonian (11) becomes (by selecting only the resonant contributions or in other words, by averaging over the fast angle θ')

$$\begin{aligned} \mathcal{H}_{1:1} = & -\frac{\mu^2}{2L'^2} - R_e^2 \frac{\mu^4}{L'^6} \left\{ C_{20} \frac{\frac{3}{4} \sin^2 i - \frac{1}{2}}{(1-e^2)^{\frac{3}{2}}} \right. \\ & \left. + \frac{3}{4}(1 + \cos i)^2 \left(1 - \frac{5}{2}e^2 + \frac{13}{16}e^4 + \dots \right) (C_{22} \cos(2\sigma) + S_{22} \sin(2\sigma)) \right\} - \dot{\theta} L'. \end{aligned} \quad (14)$$

Λ' is now constant and dropped. During the research stages, the orbit of Dawn is assumed circular ($e = 0$).

4.2.1 Circular equatorial case: $e = 0$, $i = 0$

In the circular ($e = 0$) equatorial ($i = 0^\circ$) case, the Hamiltonian (14) becomes

$$\mathcal{H}_{1:1} = -\frac{\mu^2}{2L'^2} - R_e^2 \frac{\mu^4}{L'^6} \left\{ -\frac{1}{2}C_{20} + 3(C_{22} \cos(2\sigma) + S_{22} \sin(2\sigma)) \right\} - \dot{\theta}L'. \quad (15)$$

Let us note that the eccentricity and the inclination stay constant because the Hamiltonian does not explicitly depend on the associated angles ω and Ω .

Scheeres (1994) studied the stability of bodies in orbits which are near-synchronous with the asteroid (central body) rotation. If the asteroid is of type I, like Vesta, then the stationary orbit contains two stable and two unstable equilibria. If the asteroid is of type II, the motion associated with near synchronous orbit is always unstable.

Two stable equilibria¹ $(\sigma_{s1}^*, L_{s1}^*)$, $(\sigma_{s2}^*, L_{s2}^*)$ as well as two unstable equilibria $(\sigma_{u1}^*, L_{u1}^*)$, $(\sigma_{u2}^*, L_{u2}^*)$ are found to be solutions of

$$\frac{\partial \mathcal{H}}{\partial L'} = \frac{\partial \mathcal{H}}{\partial \sigma} = 0. \quad (16)$$

The values of $\sigma_{s_i}^*$ and $\sigma_{u_i}^*$ are

$$\sigma^* = \frac{1}{2} \arctan \left(\frac{S_{22}}{C_{22}} \right) + k \frac{\pi}{2}, \quad k \in \{0, 1, 2, 3\}. \quad (17)$$

This formula remains valid for any value of C_{22} and S_{22} . For the particular value of Vesta², $C_{22} = 3.079667257459264 \times 10^{-3}$ and $S_{22} = 0$ (Tricarico and Sykes, 2010), we obtain:

$$\sigma_{s1}^* = \pi/2, \quad \sigma_{s2}^* = 3\pi/2 \quad \text{and} \quad \sigma_{u1}^* = 0, \quad \sigma_{u2}^* = \pi. \quad (18)$$

The corresponding equilibria in semi-major axis, depending on these values and on the value of C_{20} , are the solutions L'^* of the equation:

$$\dot{\theta}L'^7 - L'^4 \mu^2 - \frac{3}{2} \mu^4 R_e^2 \left(C_{20} \pm 3 \frac{C_{22}^2 + S_{22}^2 |C_{22}|}{\sqrt{C_{22}^2 + S_{22}^2}} \right) = 0. \quad (19)$$

The sign + or - corresponds respectively to the unstable and the stable points. The solutions of this equation are given in Tab. 4. We point out

¹The subscript s for stable and u for unstable.

²The corresponding normalized coefficient is equal to $\bar{C}_{22} = 0.004771$.

that to neglect the C_{20} term leads to an error spread from 9.5 to 31.9 km with a mean value of about 20.7 km on the location of the equilibria i.e. a relative variation of $\sim 3.76\%$. For comparison, this difference is about 500 m for a GEO i.e. a relative variation of 0.001%.

Table 4: The circular equatorial case: semi-major axis location of the equilibria (stable $a_{s1}^* = a_{s2}^* \stackrel{not.}{=} a_s^*$ and unstable $a_{u1}^* = a_{u2}^* \stackrel{not.}{=} a_u^*$) of the 1:1 resonance (second and third columns) with respect to the value of C_{20} (non-normalized coefficient). In fourth and fifth columns the analytical calculation of the period (20) of the resonant angle at the stable equilibrium and of the aperture (22) of the resonance.

C_{20}	a_u^* (km)	a_s^* (km)	Period (day)	Aperture (km)
0	544.436	556.529	1.216 896	134.091
$-6.872\ 554\ 928 \times 10^{-2}$	576.353	566.066	1.254 289	125.726
Difference	31.917	9.537	134.614 h	-8.365

We are now interested in the period of the resonant angle at the stable equilibrium (σ_s^*, a_s^*). This is done by linearizing in a neighborhood of the equilibrium. Then the Hamiltonian close to the equilibrium is an harmonic oscillator that can be expressed in action-angle variables and the frequency at the stable equilibrium (the subscript *eq.* means “evaluated at the equilibrium”) is given by:

$$\dot{\sigma} = \sqrt{\left. \frac{\partial^2 \mathcal{H}}{\partial L'^2} \right|_{eq.} \left. \frac{\partial^2 \mathcal{H}}{\partial \sigma^2} \right|_{eq.}} \quad \text{and} \quad T = 2\pi/\dot{\sigma}. \quad (20)$$

The values of the period of the resonant angle at the equilibrium are gathered in Tab. 4. By a similar approach, we can easily estimate the width of the resonant zone; we take the Hamiltonian level curve corresponding to one of the unstable equilibria L_u^* and σ_u^* noted \mathcal{H}_u^* that we equal to the generic Hamiltonian (15) giving the dynamics σ and L' along that curve:

$$\mathcal{H}_u^* = -\frac{\mu^2}{2L'^2} - R_e^2 \frac{\mu^4}{L'^6} \left\{ -\frac{1}{2}C_{20} + 3(C_{22} \cos(2\sigma) + S_{22} \sin(2\sigma)) \right\} - \dot{\theta}L'. \quad (21)$$

For $\sigma = \sigma_s^*$, we find the maxima (L_{\max}^*) and minima (L_{\min}^*) of this banana-curve. We obtain the width of the banana at the stable points:

$$\Delta L = L_{\max}^* - L_{\min}^*, \quad (22)$$

i.e. the aperture of the resonant zone summarized in Tab. 4.

4.2.2 Circular polar case: $e = 0, i = \pi/2$

The orbit of Dawn is polar and we have seen that the inclination does not differ much from 90° for all the radial distances from the center of Vesta (Section 3.1), so let us fix $i = \pi/2$.

The methods to find the location of the equilibria, the period at the equilibria and the aperture of the resonance are similar to that used for the equatorial case (4.2.1).

In the circular polar case, the Hamiltonian (14) becomes

$$\mathcal{H}_{1:1} = -\frac{\mu^2}{2L'^2} - R_e^2 \frac{\mu^4}{L'^6} \left\{ \frac{1}{4} C_{20} + \frac{3}{4} (C_{22} \cos(2\sigma) + S_{22} \sin(2\sigma)) \right\} - \dot{\theta} L'. \quad (23)$$

The σ location of the equilibria is always given by Eq (17), i.e. for the particular value of Vesta

$$\sigma_{s1}^* = \pi/2, \quad \sigma_{s2}^* = 3\pi/2 \quad \text{and} \quad \sigma_{s1}^* = 0, \quad \sigma_{s2}^* = \pi. \quad (24)$$

The values of the location, period and aperture are gathered in Tab. 5.

We bring to the fore that, for an inclination of 90° , the period at the stable equilibria and the aperture (Tab. 5) of the resonance are respectively equal to the double and the half of the equatorial results (Tab. 4). The doubling of the period can be easily understood regarding the equations (15), (23) and (20): in the Hamiltonian (23) a $\frac{1}{4}$ factor appears, just before the C_{22} term, (that does not exist in the Hamiltonian (15)) that becomes $\frac{1}{2}$ after the square root of the frequency equation (20), which gives a factor 2 for the period. The aperture can be explained in a similar way.

We also point out that the location of the resonance is shifted of ~ 7 km from the equatorial case for $C_{20} = 0$ and of ~ 30 km for $C_{20} \neq 0$. If we neglect the C_{20} term, we introduce an error of about 2.6 km on the aperture of the resonance and of about 11.8 km on the location of the equilibria. This last result coincides well with the 11.2 km numerically found in Tab.2.

A comparison of the analytical results with the numerical ones shows a good agreement (Tab. 1, 2 and 5). The difference between the numerical and the analytical results comes from the approximation of the osculating elements by the mean keplerian ones. The different apertures of the resonances should also come from contributions that have been neglected or averaged in the analytical study.

Table 5: The circular polar case: semi-major axis location of the equilibria (stable and unstable) of the 1:1 resonance (second and third column) with respect to the value of C_{20} . In fourth and fifth columns analytical calculating of the period of the resonant angle at the stable equilibrium and of the aperture of the resonance respectively. We also recall a part of the results of the Tab. 1 and the Tab. 2. for comparison.

C_{20}	a_u^* (km)	a_s^* (km)	Period (day)	Aperture (km)
0	552.133	549.113	2.448 927	66.699
$-6.872 554 928 \times 10^{-2}$	540.494	537.159	2.411 514	69.363
Difference	-11.639	-11.957	-134.686 <i>h</i>	2.664
Num. model	Mean of the s.m.a.		Period (day)	Aperture (km)
J_{22}	549.63		2.45	66.6
$J_{22} + C_{20}$	538.42		2.47	65.2
Until degree & order 4	538.89		2.56	63

4.2.3 Addition of C_{40}

Table 6: For the equatorial (noted Eq.) and the polar (noted Pol.) cases: semi-major axis location of the stable equilibria of the 1:1 resonance, period of the resonant angle at the stable equilibrium and aperture of the resonance with respect to the terms used in the Hamiltonian.

Term		a_s^* (km)	Period (day)	Aperture (km)
$C_{22} + C_{20}$	Eq.	566.066	1.254 289	125.726
	Pol.	537.159	2.411 514	69.363
$C_{22} + C_{20} + C_{40}$	Eq.	567.035	1.253 964	125.175
	Pol.	537.671	2.410 739	69.177

We have seen that the addition of the C_{20} term has a strong influence on the location of the resonance. Then, here, we test the effect of the C_{40} term:

$$\mathcal{H}_{J_{44}} = \mathcal{H}_{1:1} - R_e^4 \frac{\mu^6}{L^{10}} \left(\frac{105}{64} \sin^4 i - \frac{15}{8} \sin^2 i + \frac{3}{8} \right) \left(1 + \frac{3}{2} e^2 \right) C_{40}. \quad (25)$$

We summarize the values of the location, period and aperture in Tab. 6. We

can see that this term does not significantly affect the results.

4.2.4 Effect of the error on the coefficient C_{22} and C_{20}

It can be shown (Balmino, 1994) that

$$-J_2 = C_{20} = \frac{1}{5R_e^2} \left(c^2 - \frac{a^2 + b^2}{2} \right) \quad \text{and} \quad C_{22} = \frac{1}{20R_e^2} (a^2 - b^2), \quad (26)$$

where a, b and c (with $a \leq b \leq c$) are the semi-axes of the asteroid and R_e is the mean equatorial asteroid radius. If we take the values of a, b, c, R_e of Tricarico and Sykes (2010):

$$a = 289 \pm 5 \text{ km}, \quad b = 280 \pm 5 \text{ km}, \quad c = 229 \pm 5 \text{ km}, \quad R_e = 300 \text{ km}, \quad (27)$$

then the error on the value of C_{20} and C_{22} is

$$\frac{\Delta C_{20}}{C_{20}} = 18\% = \frac{\Delta \bar{C}_{20}}{\bar{C}_{20}} \quad \text{and} \quad \frac{\Delta C_{22}}{C_{22}} = 111\% = \frac{\Delta \bar{C}_{22}}{\bar{C}_{22}}. \quad (28)$$

If we slightly change the reference value R_e or if we add an error (e.g. ± 5 km) on this reference radius, the results (28) are similar. The second value of (28) can be surprising but it gives an idea of the boundary on the values of C_{22} . Owing to the supposed constant density of the asteroid, the C_{22} coefficient is assumed to be positive. Then the minimal (non null) value of C_{22} is arbitrarily chosen equal to 11% of the initial value of C_{22} . So, we calculate the extremal values and for each of them we analytically evaluate the position (semi-major axis) of the 1:1 resonance (19), the period at the equilibrium (20) and the aperture of the resonance (22) for the polar circular case. The results are presented in Tab. 7. The location in semi-major axis is between 532 and 541 km. On one hand, for a chosen value of \bar{C}_{22} , the maximum errors on the evaluation of the position of the resonance, of the period and of the aperture are respectively equal to 4.6 km, 0.04 d and 1 km, due to the error on the \bar{C}_{20} . On the other hand, for a fixed value of \bar{C}_{20} , the extremal values of \bar{C}_{22} produce errors equal to 3.5 km, 5.6 days and 78 km. So it is very important to increase the accuracy on the estimation of the three semi-axes (a, b, c). Now if we suppose this improvement, for example an error of ± 1 km on a, b and c , the error on \bar{C}_{20} and \bar{C}_{22} becomes respectively 4% and 22%. Then the extremal values for the location, period and aperture are [536.28 – 538.031] km, [2.181 – 2.733] days and [61.128 – 76.780] km.

Table 7: The circular polar case: analytical values of the location (semi-major axis noted s.m.a.) of the stable equilibrium of the 1:1 resonance (s. s.m.a), of the period at the equilibrium (T) and of the aperture (Apert.) of the resonance with respect to the extremal values of the \bar{C}_{20} and \bar{C}_{22} . The middle column and the middle line (T&S) are calculated with the values of \bar{C}_{20} and \bar{C}_{22} used in this paper and found in Tricarico and Sykes (2010). We emphasized the T&S (blue), maximum (red) and minimum (green) values obtained for the semi-major axis location, the period and the aperture.

		Min.	T&S	Max.	
$\bar{C}_{22} \backslash C_{20}$		-0.025 203	-0.030 735	-0.036 267	
Min.	5.248×10^{-4}	540.870	538.655	536.397	s. s.m.a. (km)
		7.305	7.284	7.264	T (d)
		22.793	22.964	23.142	Apert. (km)
T&S	0.004 771	539.402	537.159	534.871	s. s.m.a. (km)
		2.418	2.412	2.405	T (d)
		68.841	69.363	69.906	Apert. (km)
Max.	0.010 067	537.545	535.265	532.938	s. s.m.a. (km)
		1.661	1.656	1.652	T (d)
		100.221	100.991	101.194	Apert. (km)

4.3 Resonance 1:2, 2:3 and 3:2 in the polar case

For the 1:2, 2:3 and 3:2 resonance cases (in the circular polar case), we proceed in the same way as in the 1:1 resonance case to find the Hamiltonian, the location of the equilibria, the periods at the stable equilibria and the aperture of the resonances.

First, for each of the resonances (1:2, 2:3 and 3:2), we determine the values of the integers n, m, p, q to obtain the resonance $q_1 : q_2$ to get Kaula gravitational argument including the resonant angle $\sigma = q_2\lambda - q_1\theta$. In Tab. 8, we gather the resonances, the combinations n, m, p, q , the associated resonant angles, the Kaula gravitational arguments and the functions $F_{nmp}(i)$ and $G_{npq}(e)$ respectively evaluated at $i = \pi/2$ and $e = 0$.

Second, thanks to this combination of n, m, p, q , we determine the dif-

Table 8: Expression of the resonant angles σ , the Kaula gravitational arguments $\Theta_{n,m,p,q}$, the functions $F_{nmp}(i = \pi/2)$ and $G_{npq}(e = 0)$ with respect to the values of $n, m, q = 0$ for the resonant case $q_1 : q_2$.

$q_1 : q_2$	n	m	p	q	σ	Θ_{nmpq}	$F_{nmp}(i = \pi/2)$	$G_{npq}(e = 0)$
1:2	4	1	1	0	$2(\Omega + \omega + M) - \theta$	$\sigma - \Omega$	5/16	1
2:3	3	2	0	0	$3(\Omega + \omega + M) - 2\theta$	$\sigma - \Omega$	15/8	1
3:2	4	3	1	0	$2(\Omega + \omega + M) - 3\theta$	$\sigma + \Omega$	105/8	1

ferent sets of canonical variables, equivalent to Eq. (13), for each resonance:

$$\text{Resonance 1:2} \quad \sigma = 2\lambda - \theta, \quad L = 2L', \quad \theta' = \theta, \quad \Lambda = \Lambda' - L' \quad (29)$$

$$\text{Resonance 2:3} \quad \sigma = 3\lambda - 2\theta, \quad L = 3L', \quad \theta' = \theta, \quad \Lambda = \Lambda' - 2L' \quad (30)$$

$$\text{Resonance 3:2} \quad \sigma = 2\lambda - 3\theta, \quad L = 2L', \quad \theta' = \theta, \quad \Lambda = \Lambda' - 3L' \quad (31)$$

Then we can write the Hamiltonians associated to these resonances:

$$\begin{aligned} \mathcal{H}_{1:2} = & -\frac{\mu^2}{8L'^2} - \frac{\mu^4 R_e^2 C_{20}}{256 L'^6} \\ & - \frac{5}{16384} \frac{\mu^6 R_e^4}{L'^{10}} \left(-S_{41} \cos(\sigma - \Omega) + C_{41} \sin(\sigma - \Omega) \right) + \dot{\theta}(\Lambda' - L') \end{aligned} \quad (32)$$

$$\begin{aligned} \mathcal{H}_{2:3} = & -\frac{\mu^2}{18L'^2} - \frac{\mu^4 R_e^2 C_{20}}{2916 L'^6} \\ & - \frac{5}{17496} \frac{\mu^5 R_e^3}{L'^8} \left(-S_{32} \cos(\sigma - \Omega) + C_{32} \sin(\sigma - \Omega) \right) + \dot{\theta}(\Lambda' - 2L') \end{aligned} \quad (33)$$

$$\begin{aligned} \mathcal{H}_{3:2} = & -\frac{\mu^2}{8L'^2} - \frac{\mu^4 R_e^2 C_{20}}{256 L'^6} \\ & - \frac{105}{8192} \frac{\mu^5 R_e^4}{L'^{10}} \left(-S_{43} \cos(\sigma + \Omega) + C_{43} \sin(\sigma + \Omega) \right) + \dot{\theta}(\Lambda' - 3L'). \end{aligned} \quad (34)$$

In comparison to the Hamiltonian (23), the term in front of the cosine is $-S_{nm}$ instead of C_{nm} . That is due to the odd value of the $n - m$ ($4 - 1 = 3$, $3 - 2 = 1$, $4 - 3 = 1$) taking place in equation (6).

With the same procedure as in the 1:1 resonance, we can determine the

position of the stable equilibria in the σ variable:

$$\text{Reso. 1:2} \quad \sigma_s = \Omega - \arctan\left(\frac{C_{41}}{S_{41}}\right) + (2k + 1)\pi \quad (35)$$

$$\text{Reso. 2:3} \quad \sigma_s = \Omega - \arctan\left(\frac{C_{32}}{S_{32}}\right) + 2k\pi \quad (36)$$

$$\text{Reso. 3:2} \quad \sigma_s = -\Omega - \arctan\left(\frac{C_{43}}{S_{43}}\right) + (2k + 1)\pi \quad (37)$$

and the unstable equilibria:

$$\text{Reso. 1:2} \quad \sigma_u = \Omega - \arctan\left(\frac{C_{41}}{S_{41}}\right) + 2k\pi \quad (38)$$

$$\text{Reso. 2:3} \quad \sigma_u = \Omega - \arctan\left(\frac{C_{32}}{S_{32}}\right) + 2(k + 1)\pi \quad (39)$$

$$\text{Reso. 3:2} \quad \sigma_u = -\Omega - \arctan\left(\frac{C_{43}}{S_{43}}\right) + 2k\pi. \quad (40)$$

For clarity, we give the mean longitudes corresponding to the stable equilibria (λ_s), in degrees:

$$\text{Reso. 1:2} \quad \lambda_s = 129.05^\circ + \frac{\theta + \Omega}{2} + k 180^\circ, \quad k \in \{0, 1\} \quad (41)$$

$$\text{Reso. 2:3} \quad \lambda_s = 26.45^\circ + \frac{2\theta + \Omega}{3} + k 120^\circ, \quad k \in \{0, 1, 2\} \quad (42)$$

$$\text{Reso. 3:2} \quad \lambda_s = 47.47^\circ + \frac{3\theta - \Omega}{2} + k 180^\circ, \quad k \in \{0, 1\} \quad (43)$$

The values of the locations, periods and apertures of the resonances are summarized in Tab. 9.

We notice that, if we neglect the C_{20} terms, we introduce a mean error of ~ 11 km on the location of the resonances, of ~ 0.5 days on the periods at the stable equilibria and of ~ 2 km on the apertures of the resonances. If we compare (location and aperture) these analytical results with the numerical results (Tab. 1 repeated in the Tab. 9), we point out that the analytical results are adequate.

5 Increase of the eccentricity in the 2:3 resonance

In section 4, we have analytically found the positions of the main resonances, their apertures and their periods at the stable equilibria. As shown in Fig. 4,

Table 9: The circular polar case: resonances 1:2, 2:3 and 3:2. Values of the semi-major axis location (stable and unstable equilibria), the period of the resonant angle at the stable equilibrium and the aperture of the resonance with respect to the terms used in the Hamiltonian. For comparison, the results of the numerical test of the Tab. 1 (noted by Num. in the first column) are recalled.

Reso.		a_u^* (km)	a_s^* (km)	Period (day)	Aperture (km)
1:2	$C_{20} = 0$	874.090	874.057	76.341 231	6.796
	$C_{20} \neq 0$	866.882	866.847	75.251 862	9.953
	Num.	871.5		--	7.5
2:3	$C_{20} = 0$	721.698	721.365	9.755 028	21.953
	$C_{20} \neq 0$	712.898	712.541	9.608 888	22.575
	Num.	717.3		--	22.5
3:2	$C_{20} = 0$	420.508	419.911	4.147 596	20.056
	$C_{20} \neq 0$	404.528	403.755	3.885 027	22.401
	Num.	409.1		--	18

the ground-track resonances show an oscillation of the semi-major axis and of the resonant angle. This is why, in the left panel of Fig. 2, we see an increase of the variation of the semi-major axis exactly at the initial semi-major axis, corresponding to the ground-track resonances. Up to now we have not explained that the strongest perturbations on the radial distance come from the 2:3 resonance (right panel of Fig. 2). In this section, we investigate this phenomenon.

We make a huge number of numerical tests but we present here only the significant ones. In Fig. 5, we report the results of a numerical integration for a set of 34920 orbits, propagated over a time span of 1 year. We consider a set of initial conditions defined by a mean anomaly grid of 1° and a semi-major axis grid of 400 m, spanning the [700, 738.8] km range around the 2:3 resonance. The other fixed initial conditions are $i_0 = 90^\circ$ for the inclination, $\Omega = \omega = 0^\circ$ for the longitude of the ascending node and the argument of pericenter, and $\theta = 0^\circ$ for the sidereal time. The color code represents the maximal value of the eccentricity variation ($e_{\max} - e_{\min}$) during the integration.

In the left panel of Fig. 5, we only use the J_{32} term to modelize the central body. As expected by Eq. (42), we see three pendulum-like phase spaces. In the central panel, we add the J_2 and the J_{22} terms. We notice that

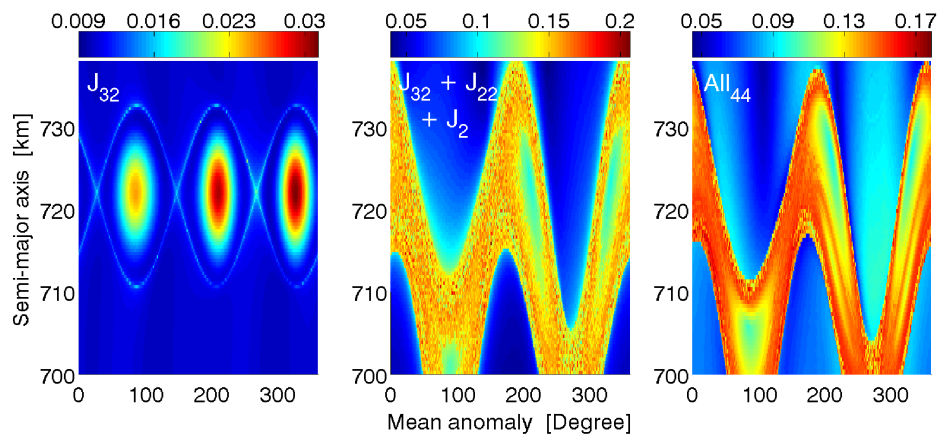


Figure 5: Around the 2:3 ground-track resonance. The amplitude of variation of the eccentricity computed as a function of the initial mean anomaly and the initial semi-major axis. The anomaly step is 1° and the semi-major axis step is 400 m. The initial conditions are $i_0 = 90^\circ$, $\Omega = \omega = 0^\circ$ and $\theta = 0^\circ$. The integration time is 1 year. The equations of motion include the central body attraction, the harmonic J_{32} in the left panel; the harmonics J_{22} and J_{32} in the central panel; and all of the harmonics until degree and order 4 (All_{44}) in the right panel.

the eccentricity reaches higher values. In the right panel, the gravity field contains all of the terms until degree and order 4. The results are similar to these of the central panel. Then, with the help of Fig. 2 and Fig. 5, we can conclude that the high value of the amplitude of variation of the radial distance that we see in Fig. 2 is due to an increase of the eccentricity in the 2:3 resonance. We can also deduce from Fig. 5 that the major part of this increase of the eccentricity is due to the J_{22} coefficient.

Now we analytically justify the fact that the first coefficient of the gravity field involving the eccentricity is the J_{22} term. First, we determine the values of the integers n, m, p, q to obtain the 2:3 resonance. Second, we only keep the non-null Kaula gravitational argument including the resonant angle $\sigma = 3\lambda - 2\theta$. In Tab. 10 we present the combinations n, m, p, q , the associated Kaula gravitational argument and the functions $F_{nmp}(i)$ (evaluated at $i = \pi/2$) and $G_{npq}(e)$.

Table 10: Expression of the functions $\Theta_{nmpq} \neq 0$, $F_{nmp}(i = \pi/2)$ and $G_{npq}(e)$ with respect to the values of n, m, p, q for the resonance 2:3.

n	m	p	q	Θ_{nmpq}	$F_{nmp}(i = \pi/2)$	$G_{npq}(e)$
2	2	0	1	$3\lambda - 2\theta - \omega - \Omega$	3/4	$7e/2 - 123e^3/16 + \dots$
3	2	0	0	$3\lambda - 2\theta - \Omega$	15/8	$1 - 6e^2 + 423e^4/64 + \dots$
4	2	0	-1	$3\lambda - 2\theta + \omega - \Omega$	-105/32	$-3e/2 + 75e^3/16 + \dots$
4	2	1	1	$3\lambda - 2\theta - \omega - \Omega$	-15/8	$9e/2 - 3e^3/16 + \dots$

The first line contains the first function G_{npq} directly proportional to e , it is related to the J_{22} coefficient. The second line corresponds to the coefficient J_{32} that induces the 2:3 resonance. In this term, the eccentricity takes place at the second order e^2 . The last two lines are also directly proportional to e but, for Vesta, the coefficient C_{44} is 30 times smaller than the coefficient C_{22} .

If we add the coefficients C_{22} and S_{22} to the Hamiltonian (33) and if we keep only the zeroth and first orders in eccentricity, we obtain:

$$\begin{aligned} \mathcal{H}_{2:3} = & -\frac{\mu^2}{2L^2} - \frac{15\mu^5 R_e^3}{8L^8} \left(-S_{32} \cos(\sigma - \Omega) + C_{32} \sin(\sigma - \Omega) \right) \quad (44) \\ & - e \frac{21\mu^4 R_e^2}{8L^6} \left(C_{22} \cos(\sigma - \omega - \Omega) + S_{22} \sin(\sigma - \omega - \Omega) \right) + \dot{\theta} \Lambda. \end{aligned}$$

With this Hamiltonian we can qualitatively give the secular equation of the eccentricity $\dot{e} \approx \left| \frac{\partial \mathcal{H}}{\partial \omega} \right|$. To have an idea of the variation of the eccentricity

during the motion we can look at the \dot{e}/e value:

$$\frac{\dot{e}}{e} \approx \left| \frac{\partial \mathcal{H}}{\partial \omega} \right| \frac{1}{e} = \frac{21\mu^4 R_e^2}{8L^6} \left(C_{22} \sin(\sigma - \omega - \Omega) - S_{22} \cos(\sigma - \omega - \Omega) \right). \quad (45)$$

Then the variation of the eccentricity depends on one of the biggest coefficients of the gravity field C_{22} . For Vesta, this coefficient C_{22} is 5 times greater than the coefficient C_{32} responsible for the 3:2 ground-track resonance. We evaluate (for the values linked to Vesta), near to the 3:2 resonance, the multiplying coefficient appearing in front of the two major contributions C_{32} and C_{22} :

$$\frac{15\mu^5 R_e^3}{8L^8} C_{32} \approx 6913 \quad \text{and} \quad e \frac{21\mu^4 R_e^2}{8L^6} C_{22} \approx e 25179. \quad (46)$$

The second value is 3.6 times greater than the first. In the case of Dawn orbiting Vesta, this highlights the importance of this additional term C_{22} in the 2:3 resonance.

6 Thrust and probability of capture

Due to the low thrust propulsion, Dawn will slowly cross the different ground-track resonances previously detected. During this transit, the orbit could become chaotic, or Dawn can be trapped in a resonance.

In this section, we first reproduce the results of Tricarico and Sykes (2010) that we explore more in depth. We simulate the slow descent of Dawn from HAMO, using a thrust of 20mN, to LAMO. An initial polar circular orbit and a continuous thrusting are assumed, with the direction of the thrust opposite to that of the relative velocity of Vesta. The simulations are displayed in Fig. 6. In the right panel we draw the evolution (continued lines) of the (osculating) semi-major axis with respect to the time. The dark and light continued curves correspond to an initial mean anomaly respectively equal to 272° and 250° . On the same panel we plot with dashed lines the corresponding evolution of the **mean** semi-major axis. In the left panel, the gray background represents the eyes of the resonance 1:1. To clarify, we plot the evolution of the mean semi-major axis in the phase space (σ, a) . We notice that the capture in resonance depends on the initial mean anomaly. Actually the probability of capture depends on the phase of the resonant angle at the time of the separatrix crossing. The trapping occurs when the spacecraft crosses the 1:1 resonance near the longitude where the Vesta equatorial semi-axis is the shortest. The reason is that this is for this value

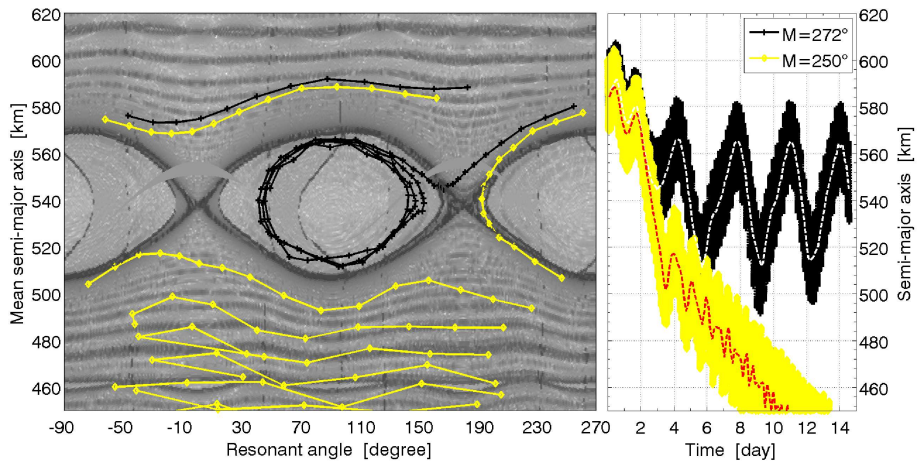


Figure 6: Evolution of Dawn from HAMO to LAMO with a thrust of -20mN with two different initial mean anomalies. In the right and left panels, the dashed lines (respectively the continued) represent the evolution of the mean semi-major axis with respect to the time (respectively to the resonant angle). In the right panel, we overlay the evolution of the osculating semi-major axis (continued lines). The trapping in the resonance 1:1 depends on the phase of the resonant angle at the time of crossing the separatrix. The force model contains the gravity field until degree and order 4 and a thrust of 20mN opposite to the Vesta rotation.

($\sigma = 90^\circ$) that we analytically find the stable point of the 1:1 resonance (Eq. 24). In Fig. 7, we plot the orbit (dark line), which leads to a capture in the 1:1 resonance, in a polar coordinate projection. We rediscover the banana curve of the Fig. 4.

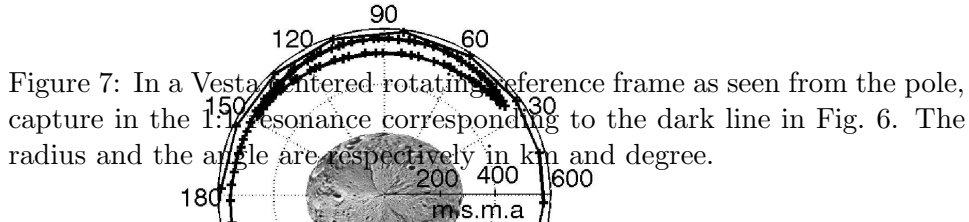


Figure 7: In a Vesta centered rotating reference frame as seen from the pole, capture in the 1:1 resonance corresponding to the dark line in Fig. 6. The radius and the angle are respectively in km and degree.

Tricarico and Sykes (2010) found, with twelve tests, that the probability of capture in the 1:1 resonance is near $1/12 \approx 8.33\%$ and they observed that higher thrusting than 50mN could exhibit a similar behavior. They also noted that the amplitude of the radial oscillations increases when crossing the 2:3 resonance, pumping up the eccentricity of the orbit. The right panel of our Fig. 2 also presents these structures and we have explained the origin of this phenomenon in the previous section. So it is possible that the increase of the eccentricity affects the probability of capture. Let us calculate the probability of capture with respect to the thrust and the initial semi-major axis. The results are presented in the Fig. 8. To obtain these figures, we take a force model that contains the gravity field until degree and order 4 and a thrust. The thrust is spread from 20mN to 36mN (to 50 for the right panel) with a step of 0.5mN. For each value of the thrust, we numerically integrate 50 times 1000 orbits with a random initial mean anomaly. In the left panel, the initial semi-major axis is equal to 1000 km corresponding to the HAMO altitude. Then these orbits cross the 2:3 resonance. In the right panel the initial semi-major axis is equal to 600 km and does not cross any resonance except the 1:1.

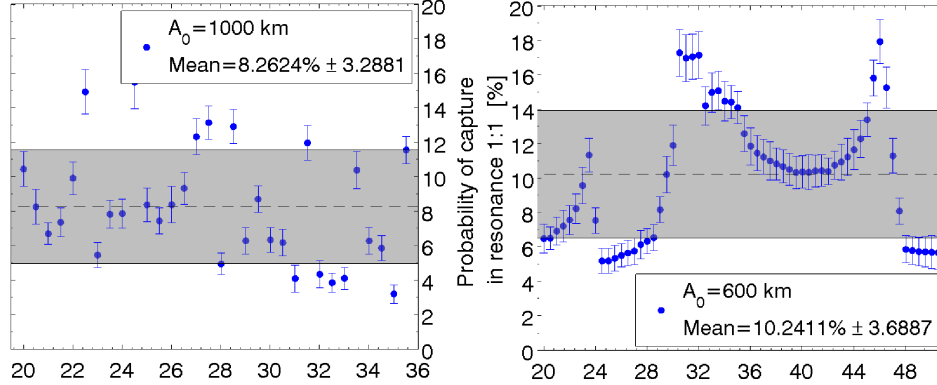


Figure 8: Probability of trapping of Dawn in the 1:1 resonance with respect to the thrust and the initial semi-major axis. For each value of the thrust we make numerical integrations with 1 000 different mean anomalies chosen randomly. We repeat this operation 50 times to obtain the means and the standard deviations.

In the left panel, we notice that the probability of capture is not linked to the value of the thrust. The mean probability of capture is equal to $8.26\% \pm 3.288$. This confirms the results of Tricarico and Sykes (2010). In the right panel, the probability of capture fluctuates between 4% and 18% with a mean equal to 10.24% and a standard deviation of 3.688 . We observe that the probability of trapping is directly linked to the value of the thrust. From a thrust equal to 48mN , the probability decreases. So, for any initial semi-major axis and mean anomaly, we advice to take a thrust between 20 and 31mN or greater than 48mN . In this way, we obtain an higher probability to cross, without permanent trapping, the 1:1 resonance.

Now, if the probe is trapped in the 1:1 resonance, it is interesting to know how we can get the probe out of the resonance. First, in Fig. 6, for the captured orbit (dark line) in the eye of the resonance, we carry on the thrust of 20mN . Thus, to escape from this resonance, we increase the value of the thrust. We decide to increase the thrust from 20 to 35mN (as Tricarico and Sykes 2010). We perform two tests where we modify the thrust at two different times: after 12 and 13 days. We note that the orbit with the change of thrust at 13 days stays in the resonance 1:1 and is closer

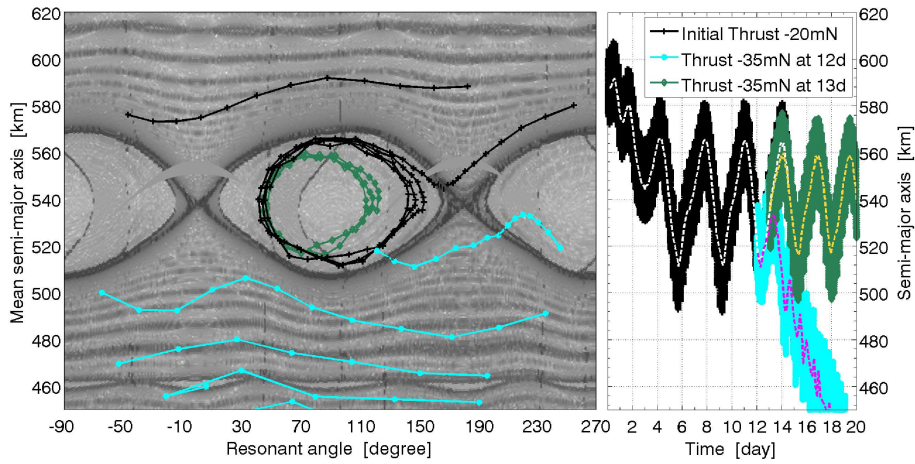


Figure 9: From a capture in the 1:1 resonance (black line), thrust of 35mN at two different times to try to escape from the trapping. The force model contains a thrust and the gravity field until degree and order 4. In right and left panels the dashed lines (respectively the continued) represent the evolution of the mean semi-major axis respectively with respect to the time and to the resonant angle. In right panel we overlay the evolution of the osculating semi-major axis. The black line correspond to the dark line of the Fig. 6. The escape from the resonance 1:1 depends on the phase of the resonant angle at the time of the operating phase (changing of the thrust).

to the center of libration. The other case escapes from the resonance. The difference in the initial time of the 35mN thrust induces a different value of the phase of the resonant angle at the time of the change of the thrust. These maps (the left panels of Figs. 9 and 6) allow us to easily understand that the probability of trapping or escape from the 1:1 resonance is dependent on the resonant angle phase.

7 Conclusions

The orbit dynamics of a polar space probe orbiting Vesta has been investigated. The proposed model includes the effects of the spherical harmonic approximation of the gravity field of the asteroid. We study the main ground-track resonances: 3:2, 4:3, 1:1, 2:3 and 1:2. We have developed a general method using an averaged Hamiltonian formulation. For each main ground-track resonance, we have analytically localized the resonance, determined the aperture and calculated the period at the stable equilibria. We have also discussed the effect of the error on the C_{20} and C_{22} coefficients on the properties of the 1:1 resonance.

Our method allows to have an analytical global approach to search all main ground-track resonances and to compute the location and the aperture of the resonances. The analytical results have been checked and validated numerically by performing numerical integrations of the complete systems.

Our theory is able to reproduce, explain and complete the results of Tricarico and Sykes (2010). The theory is general enough to be applied to a wide range of probes around any dwarf planet or most massive asteroid. In opposition to a numerical study, if the values of the spherical harmonic coefficients change (for example after new observations) our method stays valid.

In a numerical way, we have found and justify that the increase of the eccentricity in the 2:3 resonance is due to the C_{22} coefficient. We have also numerically studied the probability of trapping in the 1:1 resonance that does not depend on the thrust if the initial semi-major axis of Dawn is upper than the 2:3 resonance location. We have also showed that the phase of the resonant angle is the key during the operating phase.

Acknowledgments

Numerical simulations were made on the local computing resources (*Cluster URBM-SYSDYN*) at the University of Namur (FUNDP, Belgium).

References

- Balmino G., Gravitational potential harmonics from the shape of an homogeneous body. *Cel. Mech. Dyn. Astr.*, 60, 331-364, 1994.
- Chao, C.C., 2005. Applied orbit perturbation and maintenance. The Aerospace Press, El Segundo, California, American Institute of Aeronautics and Astronautics.
- Compere, A., Lemaître, A., Delsate, N., 2011. Detection by MEGNO of the gravitational resonances between a rotating ellipsoid and a point mass satellite. submitted to *Cel. Mech. Dyn. Astr.*
- Delsate, N., Robutel, P., Lemaître, A., Carletti, T., 2010. Frozen orbits at high eccentricity and inclination: application to Mercury orbiter. *Cel. Mech. Dyn. Astr.* 108, 275-300.
- Exertier, P., Métris, G., 1995. Semi-analytical theory of the mean orbital motion. *Astronomy & Astrophysics* 294, 278–286.
- Gedeon, G. S., 1969. Tesseral Resonance Effects on Satellite Orbits. *Cel. Mech. Dyn. Astr.* 1, 167-189.
- Hu, W., Scheeres, D.J., 2002. Spacecraft Motion About Slowly Rotating Asteroids. *Journal of Guidance, Control, and Dynamics* 25, 765-775.
- Kaula, W.M., 1966. Theory of satellite geodesy. Blaisdell Publishing Company, Waltham Massachusetts, Toronto, London.
- Lara, M., Palacián, J.F., Russell, R.P., 2010. Mission design through averaging of perturbed Keplerian systems: the paradigm of an Enceladus orbiter. *Cel. Mech. Dyn. Astr.* 108, 1–22.
- Laskar, J., 1988. Secular evolution of the Solar System over 10 million years. *Astronomy and Astrophysics* 198, 341-362.
- Laskar, J., 2005. Frequency map analysis and quasiperiodic decomposition, in Hamiltonian systems and fourier analysis: new prospects for gravitational dynamics. Benest et al. editors, Cambridge Sci. Publ., 99-129.
- Lemaître, A., Delsate, N. and Valk, S., 2009. A web of secondary resonances for large A/m geostationary debris. *Cel. Mech. Dyn. Astr.* 104, 383-402.
- Montenbruck, O., Eberhard, G., 2000. Satellite Orbits: Models, Methods, and Applications. Springer-Verlag, Berlin Heidelberg, New-York.

- Noyelles, B., Delsate, N., Carletti, T., 2011. Equilibrium search algorithm of a perturbed quasi-integrable system: NAFFO. submitted to *Physica D*.
- Pick, M., Picha, J., Vyskocil, V., 1973. *Theory of the Earth's Gravity Field*, Elsevier Sc. Pub. Co., Amsterdam, London, New-York.
- Rayman, M.D., Fraschetti, T.C., Raymond, C.A., Russel, C.T., 2006. Dawn: A mission in development for exploration of main belt asteroids Vesta and Ceres. *Acta Astronautica* 58, 605-616.
- Rossi, A., Marzari, F., Farinella, P., 1999. Orbital evolution around irregular bodies. *Earth Planets Space* 51, 1173–1180.
- Russell, C. T., Capaccioni, F., Coradini, A., de Sanctis, M. C., Feldman, W. C., Jaumann, R., Keller, H. U., McCord, T. B., McFadden, L. A., Mottola, S., Pieters, C. M., Prettyman, T. H., Raymond, C. A., Sykes, M. V., Smith, D. E., Zuber, M. T., 2007. Dawn Mission to Vesta and Ceres. Symbiosis between Terrestrial Observations and Robotic Exploration. *Earth Moon and Planets* 101, 65-91.
- Russell, R.P., Lara, M., 2009. On the design of an Enceladus science orbit. *Acta Astronautica* 65, 27–39.
- Scheeres, D.J., 1994. Dynamics about Uniformly Rotating Triaxial Ellipsoids: Applications to Asteroids. *Icarus* 110, 225-238.
- Scheeres, D.J., Ostro, S.J., Hudson, R.S., DeJong, E.M., Suzuki S., 1998. Dynamics of Orbits Close to Asteroid 4179 Toutatis. *Icarus* 132, 53–79.
- Stoer, J., Bulirsch, R., 1980. *Introduction to numerical analysis*. Springer-Verlag, New York.
- Tricarico, P., Sykes, M.V., 2010. The dynamical environment of Dawn at Vesta. *Planetary and Space Science* 58, 1516-1525.
- Valk, S., Lemaître, A., Deleflie, F., 2009. Semi-analytical theory of mean orbital motion for geosynchronous space debris under gravitational influence. *Advances in Space Research* 43, 1070-1082.
- Valk, S., Delsate, N., Lemaître, A., Carletti, T., 2009. Global dynamics of high area-to-mass ratios GEO space debris by means of the MEGNO indicator. *Advances in Space Research* 43, 1509-1526.